



# Metallic MoO<sub>x</sub> layer promoting high-valence Mo doping into CoP nanowires with ultrahigh activity for hydrogen evolution at 2000 mA cm<sup>-2</sup>

Ya-Nan Zhou<sup>a</sup>, Wen-Hui Hu<sup>b,c</sup>, Yi-Nuo Zhen<sup>a</sup>, Bin Dong<sup>a,\*</sup>, Yi-Wen Dong<sup>a</sup>, Ruo-Yao Fan<sup>a</sup>, Bin Liu<sup>a</sup>, Da-Peng Liu<sup>a</sup>, Yong-Ming Chai<sup>a,\*</sup>

<sup>a</sup> State Key Laboratory of Heavy Oil Processing, College of Chemistry and Chemical Engineering, China University of Petroleum (East China), Qingdao 266580, PR China

<sup>b</sup> Department of Chemistry, Marquette University, Milwaukee, WI 53201, United States

<sup>c</sup> X-Ray Science Division, Argonne National Laboratory, Argonne, IL 60349, United States



## ARTICLE INFO

### Keywords:

High-valence doping  
Metallic MoO<sub>x</sub>  
CoP  
Fluoroaniline  
Hydrogen evolution reaction

## ABSTRACT

High-valence metals such as Mo, W, etc. can modulate the adsorption and desorption energy of 3d-metal-based electrocatalysts, favorable for the intrinsic activity for hydrogen evolution reaction (HER) at large current density. However, the facile and exact incorporation of high-valence metals remains a big challenge. Herein, a metallic MoO<sub>x</sub> layer has been designed via anodization of Mo foil to achieve high-valence Mo doping into CoP to finally form the real active component Mo-CoP for HER. The activated metallic MoO<sub>x</sub> layer provides an optimized Mo doping into CoP, obtaining Mo-CoP/MoO<sub>x</sub> with ~226 mV (alkaline) and ~275 mV (acidic) at > 2000 mA cm<sup>-2</sup>. Meanwhile, in-situ grown F-Mo-CoP/MoO<sub>x</sub> controllable treated by fluoroaniline possesses enhanced the structural robustness of Mo-CoP/MoO<sub>x</sub> with long-term stability at large current density. This work not only illustrates the facile approach of regulating electron structure via high-valence metal doping, but it also provides the rational strategy for enhanced stability for industrial applications.

## 1. Introduction

The earth-abundant first-row (3d) transition metals with adjustable d-electron configuration have been applied to commercial water electrolysis [1–3]. And the catalytic performance of multi-metal compounds composed of 3d transition metals can be further elevated by foreign elements that can adjust the overall electronic structure of samples to modulate adsorption energies of available intermediate species [4–6]. Especially, high-valence metals (Mo [7–9], W [10–13], Ta [14,15], etc.) doping is proved to be a promising strategy to tailor 3d transition metals, such as stabilizing the valence state and improving the covalency of metal-oxygen bonds [16]. In addition, the previous work of our group also demonstrated that the doping of Mo helps to enhance the long-term stability of phosphide by tuning the bond length of the metal-phosphorus bond [9]. However, the operation temperature of many synthesis methods, including conventional hydrothermal, phosphating or vulcanization reaction, is often lower than 400 °C. In this regard, the M—O (M = Mo, W, Ta) bond of oxo acid salt is too stable to be broken, so its incorporation cannot be achieved readily.

To bridge the gap between actual operating conditions and high-

valence metals integration, the corresponding chloride or carbonyl compounds are posited as feasible alternative materials. For instance, Peng et al. employed metal dopants MoCl<sub>5</sub> and WCl<sub>6</sub> with high valence charges to adjust the 3d-metals to reduce charge transition energy, thereby improving catalytic OER performance. Similarly, Wang et al. synthesized single tungsten atoms with WCl<sub>5</sub> and loaded them on N-doped carbon materials for efficient hydrogen evolution [17]. The W-doped PtCu<sub>x</sub>Ni alloy catalyst prepared by Li et al. using W(CO)<sub>6</sub> as the W source showed expected enhancement in electrochemical surface area and mass activity [18]. Whereas MCl<sub>x</sub> and M(CO)<sub>x</sub> have contributed significantly to the provision of high-valence metals, the large-scale application has been greatly hindered due to high risk, high cost and sophisticated synthesis conditions. Therefore, it is urgently vital to develop a facile and versatile method for high-valence metal element substitution. Supported catalysts are increasingly drawing tremendous attention due to their strong modulation on the chemisorption of surface intermediates benefited from substrate and interface effects, which can remarkably accelerate reaction kinetics [19–21]. Intrinsically, in addition to conductivity, the metal substrate can also provide corresponding trace amounts of metal ions under appropriate conditions, thereby

\* Corresponding authors.

E-mail addresses: [dongbin@upc.edu.cn](mailto:dongbin@upc.edu.cn) (B. Dong), [ymchai@upc.edu.cn](mailto:ymchai@upc.edu.cn) (Y.-M. Chai).

achieving heteroatom doping. For example, Zou et al. prepared NiFe LDH with high activity and stability by means of additional Ni source and Fe ions originated from Fe foam itself [22]. Nevertheless, many metal substrates, such as Mo and W foil, consisting of desired high-valence metals, generally features high strength and are relatively inert, making it difficult for ions to escape into samples due to the dense atomic arrangement. Therefore, the surface metal atoms activation is of great significance to further motivate the interface electronic interaction and catalytic performance. It has been noted that various supports, particularly, Mo [29], W [22–24], Al [25], Ti [26,27], and Sn [28] foil, can form characteristic metal nanosheets through crystal plane exfoliation during anodization via special self-ordering phenomenon, which can be easily transformed into nanostructured compounds by post-modification. Hence, the anodized nanosheets composed of abundant activated metals reasonably make the high-valence metals doping feasible.

Parallel to activity, stability is another critical criterion and an essential precondition for practical large-scale commercial applications. At present, most electrocatalysts can only operate stably for several tens of hours or less at small current density due to undesired oxidative decomposition, metal leaching and structure collapse, which are even more severe at large current density. Earlier reports claimed that strengthened durability can be realized by elaborate coating on the catalyst surface. For example, Chen et al. encapsulated FeCoNi ternary alloy particles into N-doped graphene to improve robustness in the HER process [29]. The MOF film prepared by Fischer et al. on a conductive substrate can form an active coating after being immersed in the electrolyte to ensure stability and activity [30]. Although the coating has been effective in prolonging the life of catalysts, it is a huge challenge to select suitable coating materials and operating methods to avoid

possible activity decrease.

Herein, combined with the above analysis, ultrahigh active and robust CoP nanoneedles modulated via high-valence Mo and in situ coating (F-Mo-CoP/MoO<sub>x</sub>) are prepared for HER at large current. Firstly, a facile short-time partial anodic electrooxidation is applied to activate the metallic molybdenum (Fig. 1), which is beneficial to subsequent heteroatom integration. The facilitated water dissociation, modulated adsorption energy and electronic structure, as well as moderated d-band level via high-valence Mo are proved by subsequent corroborative experiments and calculations. Promisingly, the Mo-modulated real CoP active centers (Mo-CoP/MoO<sub>x</sub>) with optimized Mo doping exhibited boosted HER activity with current densities of  $> 2000 \text{ mA cm}^{-2}$  at  $\sim 226 \text{ mV}$  (alkaline) and  $\sim 275 \text{ mV}$  (acidic), making it potentially admirable alternatives to industrial Pt. More importantly, high stability is the prerequisite and guarantee for industrial application. Therefore, a mild in-situ polymerization strategy is crafted to enhance the robustness of Mo-CoP/MoO<sub>x</sub>, achieving extended long-term durability of 140 h.

## 2. Experimental section

### 2.1. Synthesis of MoO<sub>x</sub> and MoO<sub>2</sub>

The MoO<sub>x</sub> was synthesized by a sample anodization process. Firstly, a piece of Mo foil ( $1 \times 2 \text{ cm}$ ) was washed with hydrochloric acid, acetone, deionized water (DI-water) and absolute ethyl alcohol, respectively. Then, the electrochemical oxidation was carried out and controlled in the PBS solution at 0.5 V for 10 s, 100 s and 300 s using Mo foil, Pt foil and saturated calomel electrode (SCE) as work electrode. The anodized Mo foil was named MoO<sub>x</sub>-*t* (*t* is the oxidation time).

For comparison, the MoO<sub>2</sub> was synthesized by placing the cleaned

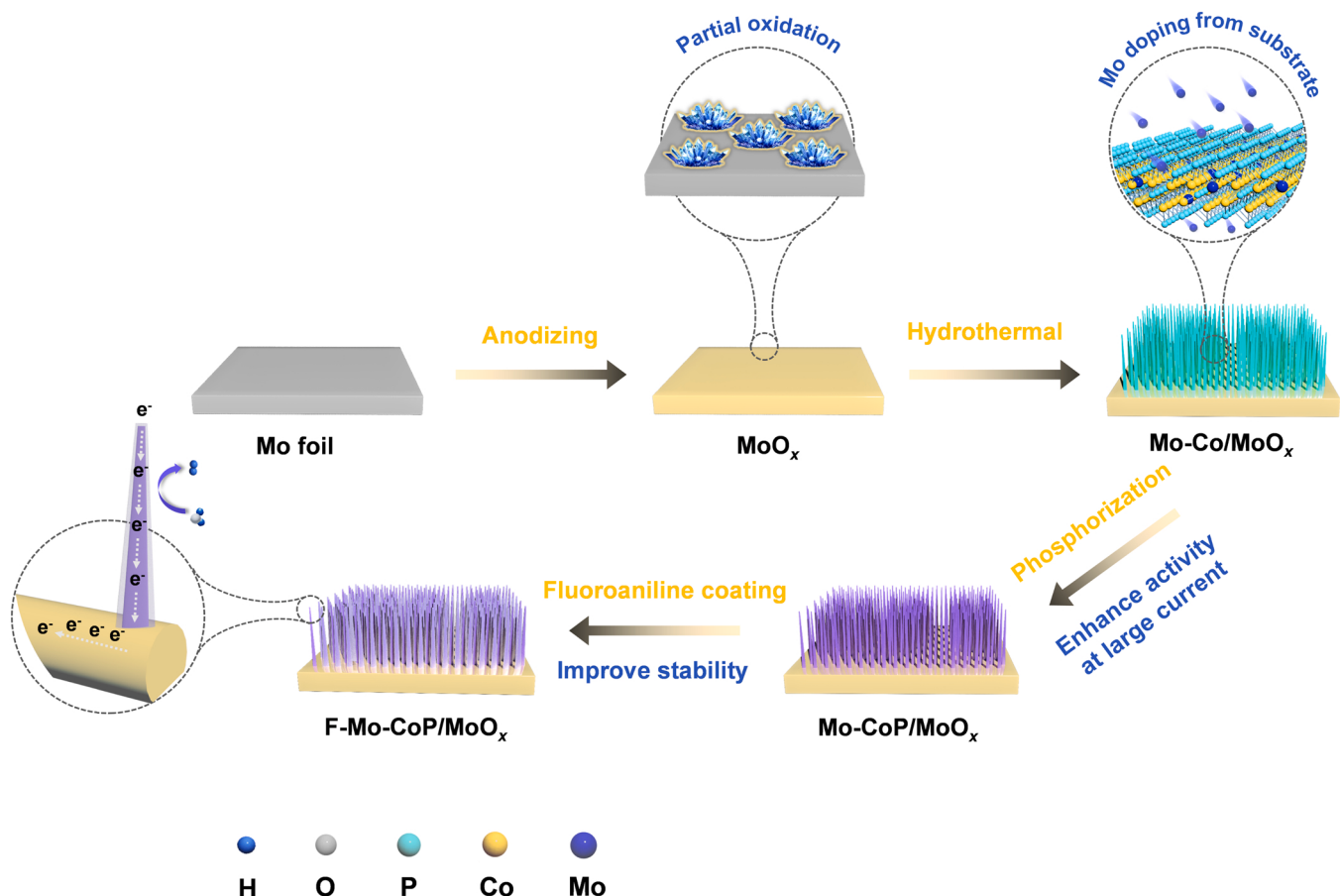


Fig. 1. Schematic illustration of the synthesis process for F-Mo-CoP/MoO<sub>x</sub> on anodized Mo foil.

Mo foil in a stainless steel autoclave containing 10 mL DI-water and 0.1 mL H<sub>2</sub>O<sub>2</sub> at 60 °C for 12 h.

## 2.2. Synthesis of Mo-Co/MoO<sub>x</sub> nanoarrays

Typically, 0.29 g CoCl<sub>2</sub>·6 H<sub>2</sub>O, 0.92 g NH<sub>4</sub>Cl and 0.37 g urea were dissolved in 20 mL DI-water and stirred for 10 min. Then the well-mixed solution and MoO<sub>x</sub> were put into a Teflon-lined stainless steel autoclave at 120 °C for 6 h. After cooling to room temperature, the Mo foil grown with Co precursor was washed with ethanol and DI-water, respectively, and then vacuum-dried for preservation.

The Mo-Co/MoO<sub>2</sub> was prepared using the same method except for MoO<sub>2</sub> as the substrate.

## 2.3. Synthesis of Mo-CoP/MoO<sub>x</sub> nanoarrays

The quartz boat loaded as-prepared Mo-CoP/MoO<sub>x</sub> or Mo-CoP/MoO<sub>2</sub>

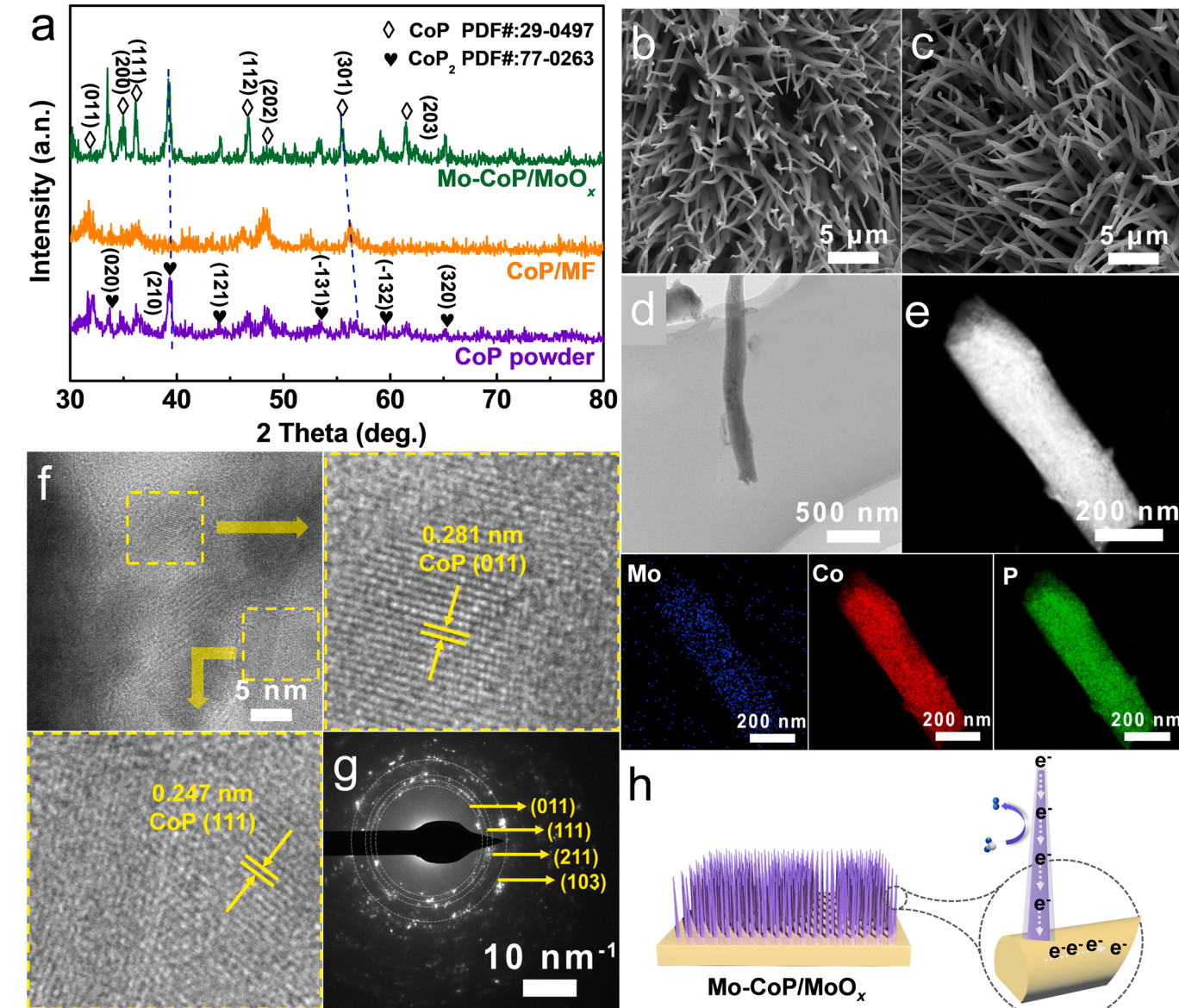


Fig. 2. Morphologies and structure characterization of Mo-CoP/MoO<sub>x</sub>-100. (a) XRD pattern of the obtained CoP powder, CoP/MF, Mo-CoP/MoO<sub>x</sub>-100. (b-c) SEM images. (d) TEM image. (e) Annual dark-field TEM image of Mo-CoP/MoO<sub>x</sub>-100 and corresponding STEM-EDX mapping of Mo, Co, P. (f) HRTEM image with a clear interface between the (011) and (111) plane of CoP and the (110) plane of Mo. (g) SAED image of Mo-CoP/MoO<sub>x</sub>-100. (h) schematic illustration of HER reaction on Mo-CoP/MoO<sub>x</sub>-100.

was placed downstream of the tube furnace and the quartz boat with 0.5 g NaH<sub>2</sub>PO<sub>4</sub> at upstream. Then the tube furnace was programmed to 300 °C with a heating rate of 2 °C min<sup>-1</sup> under Ar atmosphere. The resulting samples were denoted as Mo-CoP/MoO<sub>x</sub>-t (t is the oxidation time).

## 2.4. Synthesis of F-Mo-CoP/MoO<sub>x</sub> nanoarrays

The above Mo-CoP/MoO<sub>x</sub> was immersed in a fluoroaniline solution of 15 mL containing 0.022 g fluoroaniline for 30 s. Then the obtained sample was rinsed several times with DI-water to remove excess fluoroaniline and named F-Mo-CoP/MoO<sub>x</sub>.

### 3. Results and discussion

#### 3.1. Structure characterization

**Fig. 1** demonstrates the overall synthesis process of the final F-MoCoP/MoO<sub>x</sub>, where the pristine smooth Mo foil serves as the support and molybdenum source, as shown in **Fig. S1a**. After anodizing, the stacked Mo nanocrystalline clusters can be clearly observed on the surface of Mo foil (MoO<sub>x</sub>) (**Fig. S1b**). Different from chemical oxidation, the anodization can generate activated metallic Mo nanocrystals exfoliated along (110) crystal with partial oxidation edges, which is different from the self-ordering phenomenon seen in other anodic oxides. These Mo nanosheets can easily release Mo elements to facilitate the subsequent replacement of Co by Mo. [31]. The main substantial composition of MoO<sub>x</sub> is confirmed by X-ray diffraction (XRD). As **Fig. S2a** shows, the two characteristic peaks at 58.64° and 73.60° can be well assigned to the (200) and (211) crystal planes of metallic Mo (JCPDS No: 42-1120), and the peak at 23.83° matches well with the (020) plane of MoO<sub>3</sub> (JCPDS No: 80-0347), which, together with the absence of Mo (110) peak, implies the formation of abundant active molybdenum [31].

The detailed crystallinity and phase information on Mo-CoP/MoO<sub>x</sub> scraped from the Mo foil is also characterized by XRD. **Fig. 2a** shows that the final Mo-CoP/MoO<sub>x</sub>, CoP powder and CoP/MF which in-situ grown on pure Mo foil without anodic oxidation all compose of seven peaks around 32.1°, 35.0°, 36.2°, 46.7°, 48.4°, 55.6° and 61.6° which can be assigned to the (011), (200), (111), (112), (202), (301) and (203) crystal planes of CoP (JCPDS No: 29-0497) respectively. In addition, peaks located at 33.5°, 39.2°, 44.1°, 53.4°, 59.3° and 65.1° can be indexed to the (020), (210), (121), (-131), (-132) and (320) crystal face of CoP<sub>2</sub> (JCPDS No: 77-0263). This result suggests that Mo-CoP/MoO<sub>x</sub> is mainly comprised of CoP and CoP<sub>2</sub>. However, according to previous reports, phosphorus-rich phosphides exhibit lower electrocatalytic hydrogen evolution activity, which may be attributed to the reduced overlap of wave functions between metal atoms and P atoms [32]. Furthermore, with the increase of P content, the P-H interaction would be too strong. Hence, in this work, the active component is considered to be Mo doped CoP.

Notably, although no peaks of MoO<sub>x</sub> or MoP are observed for the scraped Mo-CoP/MoO<sub>x</sub>, the presence of MoO<sub>3</sub> is proved by the peaks at 23.2° and 26.2° for Mo-CoP/MoO<sub>x</sub> grown on Mo foil (**Fig. S2b**), suggesting that MoO<sub>x</sub> exists on the substrate. Moreover, compared with CoP powder and CoP/MF contrast samples, the diffraction peaks of resulting Mo-CoP/MoO<sub>x</sub> slightly shift to a smaller angle, consistently confirming that the Co has been partially substituted by Mo atoms. The Mo-Co/MoO<sub>x</sub> nanoneedles prepared by hydrothermal reaction show a smooth surface with a uniform diameter of around 180 nm (**Fig. S1c, d**). After phosphorization, the vertical robust Mo-CoP/MoO<sub>x</sub> manifests a similar acicular structure to pristine Co nanoarrays except for slight twists and rougher surface (**Fig. 2b, c**), conductive to available high specific surface area, fast bubbles release and effective mass transfer. In order to unveil the critical role of anodization in the vertical structure of nanoarrays, the same procedure is adopted to prepare CoP on pure Mo foil without any extra treatment (CoP/MF) (**Fig. S3**). Note that the Co/MF precursor piled up chaotically, and undesired agglomeration even occurred after phosphorization. It can be dependably chalked up to the reasons that activated metallic Mo not only protects Co nanoneedles from collapse during phosphating but also regulates the growth direction of CoP and makes it perpendicular to the target substrate [33,34]. In view of these results, we proposed that the in situ generated MoO<sub>x</sub> in Mo foil mainly acts as the Mo source to induce Mo substitution and the perpendicular growth of CoP nanorods. **Fig. 2e** shows the scanning transmission electron microscope (STEM)-energy-dispersive X-ray spectroscopy (EDX), demonstrating the nanoneedle-like CoP structure and uniformly dispersed Mo, Co and P elements with the atomic ratio of Co:P:Mo around 38:61:1 (**Table S1**). More information is provided by HRTEM (**Fig. 2f**), which displays two clear CoP crystal lattices of (011) and (111)

phases with the d-spacings of 0.281 and 0.225 nm that can be manifested by the selected area electron diffraction (SAED) image in **Fig. 2g**. It is worth mentioning that no MoP lattices are discerned, and the discernible lattice dislocations and defects are presumably due to the introduction of the relatively large-radius Mo. Further coated by poly-fluoroaniline layer via in situ polymerization, the resulting F-Mo-CoP/MoO<sub>x</sub> shows a distinct core-shell structure comprised of an amorphous shell with a thickness of ~10 nm and a CoP nanoneedle core (**Fig. S4a, b**). And the corresponding element mapping and contents over a single nano-needle further consolidate the uniform distribution of Co, Mo, P and F elements as well with the presence of fluoroaniline coatings (**Table S2**).

The surface chemical composition and strong electronic interaction of samples were revealed by X-ray photoelectron spectroscopy (XPS). **Fig. S5a** presents the XPS survey spectra of Mo-CoP/MoO<sub>x</sub>, indicating the coexistence of Mo, Co and P again. The Co 2p energy level in **Fig. 3a** of Mo-Co/MoO<sub>x</sub> shows the peak of Co<sup>2+</sup> in CoMoO<sub>4</sub> and the signals at 781.7 and 797.8 eV are the response of oxidized Co species [35]. For Mo-CoP/MoO<sub>x</sub>, the peak belonging to CoMoO<sub>4</sub> disappeared, and the Co 2p<sub>1/2</sub> and Co 2p<sub>3/2</sub> can be separated into two new typical peaks at 778.57 and 793.47 eV, respectively, which are indexed to Co-P species [36,37]. Besides, the satellite peaks (noted as Sat.) at 785.4 and 802.8 eV can be ascribed to Co<sup>2+</sup> in CoP. In addition, Co 2p peaks of Mo-CoP/MoO<sub>x</sub> show a positive shift of ~0.3 eV, implying the strong electron interaction between Co and P. Compared with pure CoP powder, Mo-CoP/MoO<sub>x</sub> is detected a negative movement (**Fig. S6a**), confirming the local modified electron density through Mo doping [40]. Moreover, the Co<sup>2+</sup>/Co<sup>3+</sup> ratio calculated by fitting Co 2p XPS peaks for Mo-CoP/MoO<sub>x</sub> is higher than that for CoP powder (**Table S3**), which further confirms the strong electronic interaction between Co, P and Mo. Various valence states of Mo can be fitted in Mo-Co/MoO<sub>x</sub> precursor (**Fig. S5b**), while the Mo 3d spectra in Mo-CoP/MoO<sub>x</sub> sample (**Fig. 3b**) can only be deconvoluted into three types Mo (Mo<sup>3+</sup>, Mo<sup>4+</sup> and Mo<sup>5+</sup>) as a result of oxidation during treatment. For P 2p spectra in **Fig. S5c**, peaks at 129.2 and 130.0 eV originate from the CoP [37,39], and the accompanied peak of oxidized P species is located at 133.9 eV [38–41]. Noticeably, the binding energies of P 2p<sub>1/2</sub> and P 2p<sub>3/2</sub> are negatively shifted (~0.39 eV) compared with pure CoP powder (**Fig. S6b**), consistent with the earlier report [38]. Further, the local electronic structure and coordination environment of Mo in Mo-CoP/MoO<sub>x</sub> are analyzed by X-ray absorption spectroscopy (XAS). **Fig. 3c** shows the detected X-ray absorption near-edge structure (XANES) of CoP and Mo-CoP/MoO<sub>x</sub>, and it can be observed that the XANES edge of Mo-CoP/MoO<sub>x</sub> shifts to lower energy compared to pure CoP, indicating a decreased oxidation of Co in synthesized Mo-CoP/MoO<sub>x</sub>, agreeing well with the XPS results. For the Fourier-transformed (FT) k<sup>3</sup>-weighted extended X-ray absorption fine structure (EXAFS) in **Fig. 3d**, the primary peak around 1.8 Å can be attributed to the Co—P bond [42]. To confirm the local coordination structure of Co, the structure model driven from the theoretical calculation is applied to fit the EXAFS spectrum of Mo-CoP/MoO<sub>x</sub>. **Fig. S7** and **Table S4** show the existence of Co—P and Co—Co bond, while no Mo—P can be assigned, which verifies Mo doped into the CoP without the generation of the new phase. The lower peak intensity of Mo-CoP/MoO<sub>x</sub> also suggests the falling coordination number of Co and distorted crystal structure after Mo incorporation [42]. These results demonstrate that Mo and P can synergistically adjust the surface electronic structure of Co species. Meanwhile, the Mo tailoring benefits to optimizing the adsorption of H\* and desorption of H<sub>2</sub> on active sites.

#### 3.2. HER performance of Mo-CoP/MoO<sub>x</sub>

Furthermore, the HER performance of Mo-CoP/MoO<sub>x</sub> was firstly investigated in 1.0 M KOH via a standard three-electrode system at ambient temperature. First of all, the electrocatalytic HER activity was optimized by adjusting the anodization degree. Three categories of electrocatalysts were obtained with the different anodizing times of Mo-

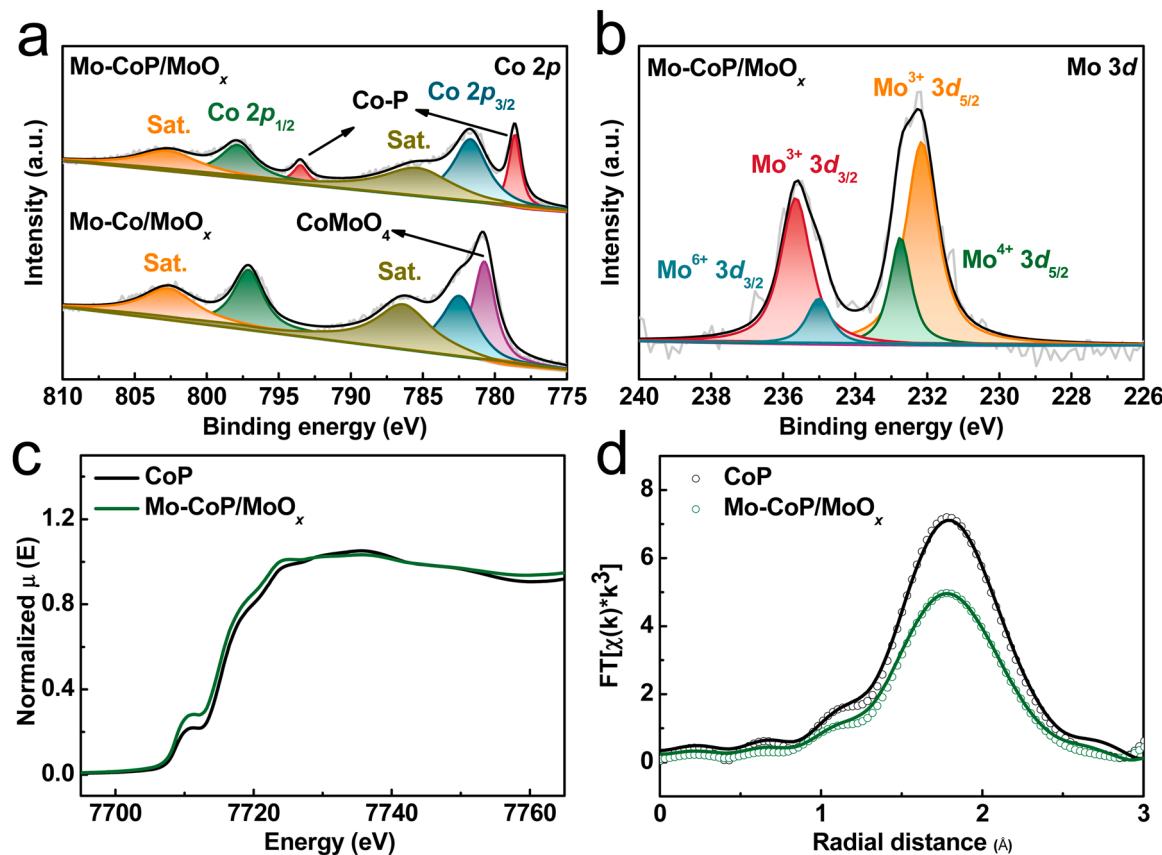


**Fig. 3.** High-resolution XPS spectra for (a) Co 2p and (b) Mo 3d of Mo-Co/MoO<sub>x</sub> and Mo-CoP/MoO<sub>x</sub>. The Co K-edge (c) XANES, and (d) EXAFS spectra of CoP, Mo-CoP/MoO<sub>x</sub>, respectively.

CoP/MoO<sub>x</sub>-*t* (*t* means 10, 100 and 300 s, respectively) and the corresponding linear-sweep voltammetry (LSV) curves are shown in Fig. S8a.

Obviously, the degree of electro-oxidation can be controlled by adjusting the oxidation time, thus affecting HER activity. Apparently, the Mo-CoP/MoO<sub>x</sub>-100 exhibits the best HER activity with the lowest overpotential. In detail, the overpotential decreases with the electro-oxidation time rising from 10 s to 100 s. The better HER activity could be a result of the regulated CoP electron density by appropriate Mo integration, which provides extra electrons to P, leading to a softer hydrogen adsorption free energy of Co sites. While as the time is further cumulative to 300 s, the HER performance deteriorates substantially instead, which is speculated to originate from the excessive introduction of Mo dopants, resulting in strong adsorption of hydrogen intermediates.

The optimized Mo-CoP/MoO<sub>x</sub>-100 is employed for the following alkaline HER research. From the polarization curves in Figs. 4a and S8b, the Mo foil, MoO<sub>x</sub> and Mo-Co/MoO<sub>x</sub>-100 show negligible HER current in the chosen potential range, while the final Mo-CoP/MoO<sub>x</sub>-100 owns the lowest overpotential of 40 and 141 mV at 10 and 200 mA cm<sup>-2</sup>, respectively. Notably, an ultrahigh current density of > 2000 mA cm<sup>-2</sup> is reached with only ~226 mV, outperforming most reported CoP-based electrocatalysts (Table S5). Comparatively, the LSV curve of CoP on Mo foil (CoP/MF) is depicted to further highlight the pivotal role of anodic oxidation and Mo incorporation. As expected, the CoP/MF requires 83 and 202 mV to drive the current density of 10 and 200 mA cm<sup>-2</sup>, inferior to Mo-CoP/MoO<sub>x</sub>-100. A similar unsatisfactory performance happens to Mo-CoP/MoO<sub>2</sub> with H<sub>2</sub>O<sub>2</sub> as an oxidation reagent (Fig. S9). Fig. 4b shows a comparison of overpotential at 10 and 100 mA cm<sup>-2</sup> between CoP grown on Mo foil with the different treatment procedures. There appear to be two primary reasons for the bewildering phenomenon: Firstly, metallic Mo stripped off via oxidation can be effectively introduced into the CoP lattice to regulate its electronic structure and

optimize the adsorption and desorption of active hydrogen intermediates. Secondly, the activated Mo species can induce the well-defined Mo-CoP/MoO<sub>x</sub> nanoneedle arrays perpendicular to substrate orderly to maximize the exposure of active sites. While for CoP/MF and Mo-CoP/MoO<sub>2</sub>, the accessible Mo species are too scarce to stimulate the vertical growth and maintain the morphology of CoP. Therefore, the disorderly CoP bundles greatly lower active sites and mass transfer, in addition to making bubbles difficult to release quickly. Tafel plots were calculated from polarization curves to bring insight into reaction kinetics and rate-determining step of HER. As shown in Fig. 4c, the Mo-CoP/MoO<sub>x</sub>-100 displays a much lower Tafel slope of 74.8 mV dec<sup>-1</sup> than Mo-Co/MoO<sub>x</sub>-100 (99.1 mV dec<sup>-1</sup>) and CoP/MF (85.3 mV dec<sup>-1</sup>), indicating that the Volmer-Heyrovsky mechanism and the Volmer step is the rate-determining step [44].

The effect of anodic oxidation on the active surface area and conductivity of the catalysts can also be reflected by electrochemical impedance spectroscopy (EIS) and electrochemical active surface area (ECSA). The Nyquist plots fitted by an equivalent circuit model in the inset of Fig. 4d illustrate the maximum conductivity of Mo-CoP/MoO<sub>x</sub>-100, consistent with the fast HER kinetics. In addition, the ECSA determined by cyclic voltammetry (CV) curves with different sweep rates is proportional to the double-layer capacitance ( $C_{dl}$ ). Fig. 4e shows no significant difference in  $C_{dl}$  value between Mo-Co/MoO<sub>x</sub>-100 (28.8 mF cm<sup>-2</sup>) and Mo-CoP/MoO<sub>x</sub>-100 (35.8 mF cm<sup>-2</sup>). However, the CoP/MF shows much lower ECSA with  $C_{dl}$  of 10.9 mF cm<sup>-2</sup> caused by the CoP stacking. It needs to be mentioned that under alkaline conditions, the P species are more inclined to dissolve than Co species during HER process, leaving metal counterparts exposed to OH<sup>-</sup> and thus forming thin Co(OH)<sub>2</sub> shell on the surface of Mo-CoP/MoO<sub>x</sub>, which also plays a crucial role in hydrogen evolution (Fig. 4f) [43]. These results demonstrate that the fast electron transfer, abundant active sites and efficient

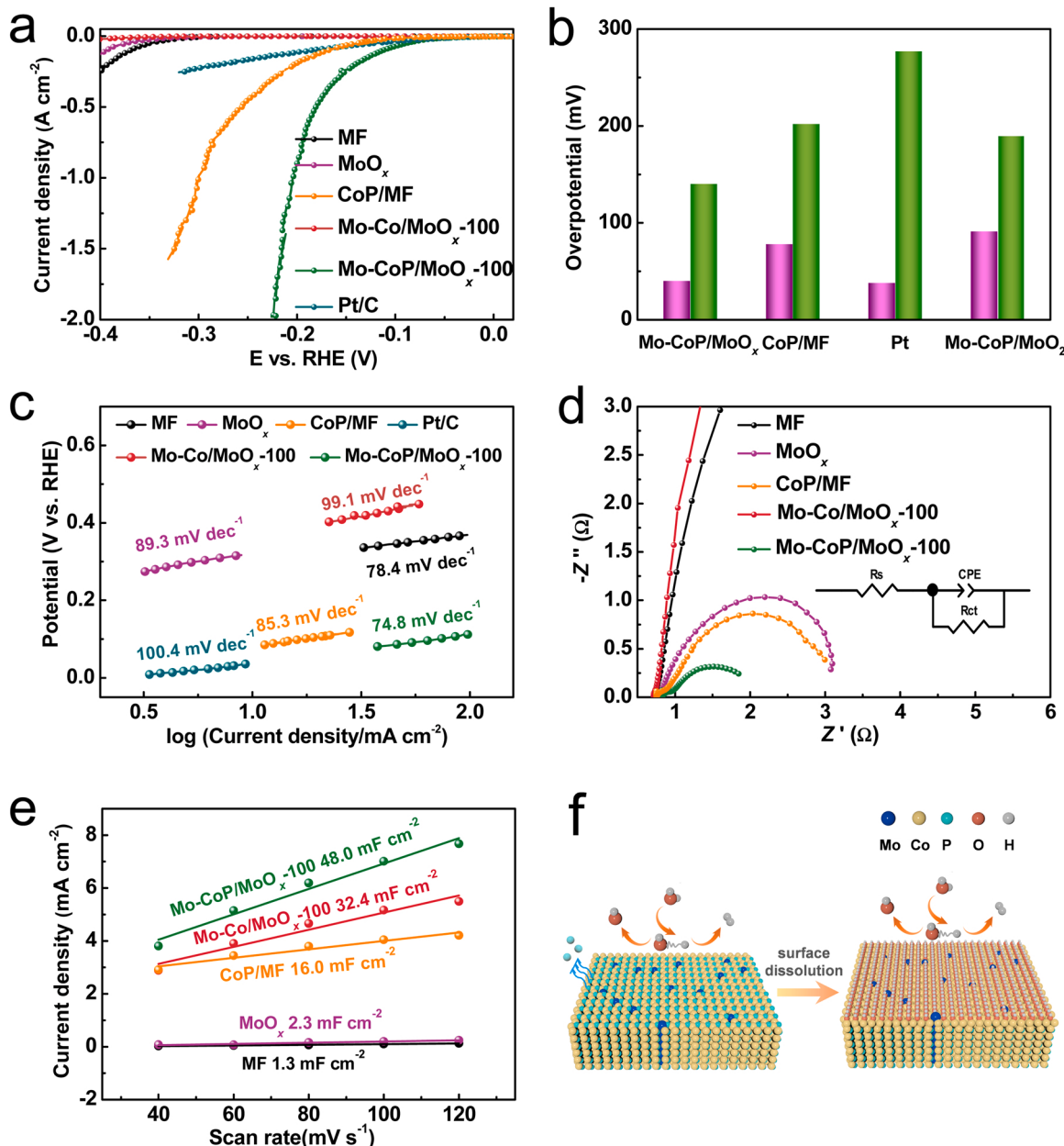


**Fig. 4.** Electrochemical measurement for HER in 1.0 M KOH. (a) LSVs, (b) Comparison of required overpotential at 10 (purple columns) and 200 mA cm<sup>-2</sup> (green columns) of Mo-CoP/MoO<sub>x</sub>-100, CoP/MF, Pt/C and Mo-CoP/MoO<sub>2</sub>. (c) Tafel plots, (d) EIS and (e)  $C_{dl}$  of MF, MoO<sub>x</sub>, CoP/MF, Mo-Co/MoO<sub>x</sub>-100, Mo-CoP/MoO<sub>x</sub>-100. (f) Illustration of dissolution and reconstruction of Mo-CoP/MoO<sub>x</sub> sample in 1.0 M KOH.

bubble release modulated by Mo doping can synergistically boost the HER activity.

As a crucial indicator of catalyst performance evaluation, the durability of Mo-CoP/MoO<sub>x</sub>-100 is prolonged by fast room-temperature fluoroaniline coating with only 30 s. The polarization curves of obtained F-Mo-CoP/MoO<sub>x</sub> were first measured and shown in Fig. 5a. As expected, a low overpotential of 43 mV is required at 10 mA cm<sup>-2</sup> with an increase of only 3 mV than Mo-CoP/MoO<sub>x</sub>-100. Encouragingly, its activity is even better than Mo-CoP/MoO<sub>x</sub>-100 at  $> 310$  mA cm<sup>-2</sup>. Besides, stability tests show that only a negligible decrease is detected before and after 3000 CV cycles with a scan rate of 60 mV s<sup>-1</sup> (Fig. 5b). Moreover, the chronoamperometry curve (Fig. 5c) at a constant potential of  $-1.16$  V vs. SCE indicates the enhanced long-term durability of 200 h for F-Mo-CoP/MoO<sub>x</sub>-100 without significant current degradation. (Fig. 5d) while the current density of Mo-CoP/MoO<sub>x</sub>-100 fluctuates inevitably with the range from 120 to 105 mA cm<sup>-2</sup> within 17 h with the

massive collapse of nanoarrays, which fail to meet the demand of commercial applications. It is worth mentioning that after the HER process, the Co 2p and Mo 3d slightly shift to higher binding energy (Fig. S10), implying the formation of higher valence Co and Mo species.

Further, the HER performance of resulting electrocatalysts was also assessed in 0.5 M H<sub>2</sub>SO<sub>4</sub>. Similarly, the optimized Mo-CoP/MoO<sub>x</sub>-100 is employed to compare catalytic performance with others (Fig. S11). Encouragingly, the Mo-CoP/MoO<sub>x</sub>-100 also presents remarkable activity with the overpotential of 62 mV and 168 mV to reach 10 and 200 mA cm<sup>-2</sup>, and a large current density of  $> 2000$  A cm<sup>-2</sup> is achieved at  $\sim 275$  mV, superior to Mo-Co/MoO<sub>x</sub>-100, CoP/MF and other Co-based catalysts (Table S6). The lower Tafel slope ( $67.2$  mV dec<sup>-1</sup>) and charge transfer resistance, as well as higher  $C_{dl}$  value ( $35.8$  mF cm<sup>-2</sup>) (Figs. S11 and S15) for Mo-CoP/MoO<sub>x</sub>-100, implies better conductivity and abundant active sites. As mentioned above, after operating for 12 h at a constant voltage of  $-0.4$  V vs. RHE (Fig. S17), the needle-shaped Mo-

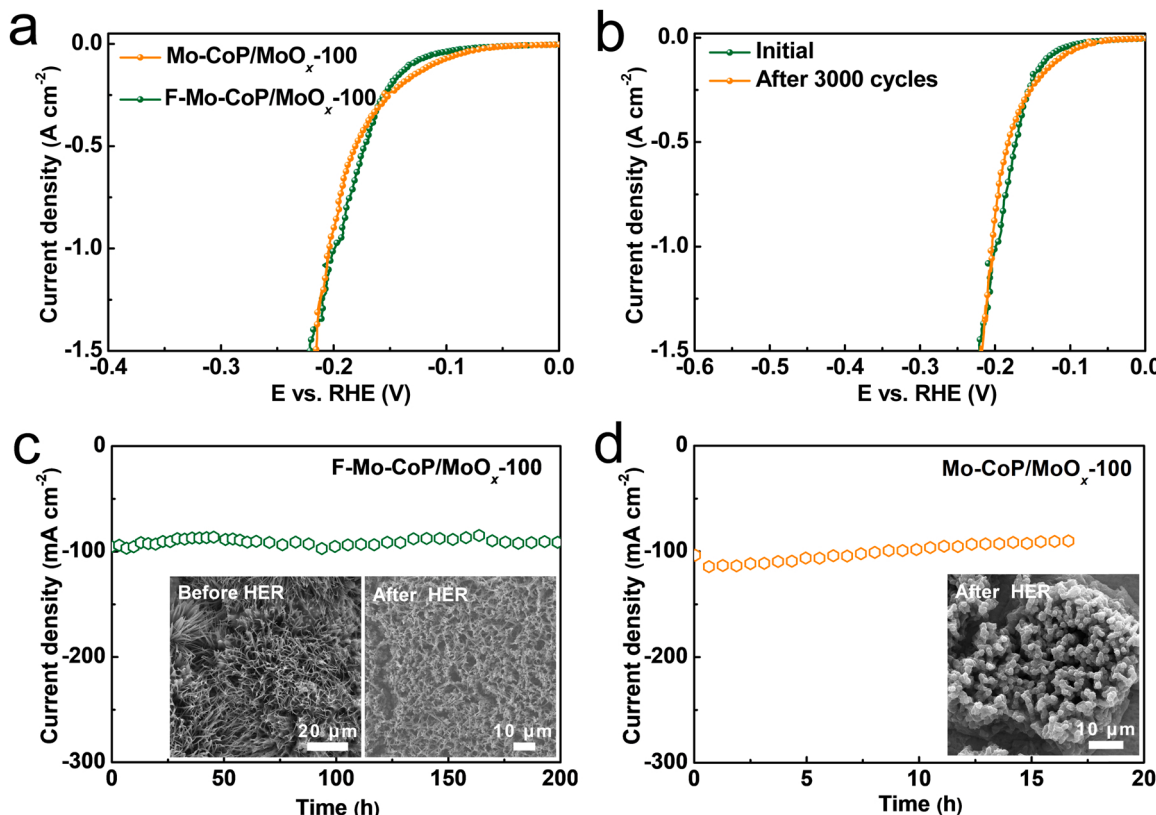


**Fig. 5.** (a) LSV curves of Mo-CoP/MoO<sub>x</sub>-100 and F-Mo-CoP/MoO<sub>x</sub>-100. (b) LSV curves before and after 3000 CV cycles of F-Mo-CoP/MoO<sub>x</sub>-100. Chronoamperometry curve for (c) F-Mo-CoP/MoO<sub>x</sub>-100 and (d) Mo-CoP/MoO<sub>x</sub>-100.

CoP/MoO<sub>x</sub>-100 crumbled thoroughly with the current density decreasing from 100 to 80.3 mA cm<sup>-2</sup>. While for F-Mo-CoP/MoO<sub>x</sub>-100, the polarization curves after 3000 cycles even showed an enhanced activity (Fig. S18b). More intriguingly, it can tolerate 200 h at the same voltage in a steady current with the CoP nanoarrays stably upright (Fig. S19). The above results reveal the high stability and the excellent HER performance benefited from Mo integration and polymerization by improving adsorption-desorption strength.

### 3.3. DFT calculations for the mechanism of HER improvement

For simplicity, the CoP and Mo doped CoP (Mo-CoP) are constructed for theory calculation. To uncover the intrinsic impact of Mo dopant on the HER activity and to obtain a deeper insight into the electrocatalytic active centers, the density of state (DOS) and *d*-band center are first calculated based on density functional theory (DFT) with simulated model structure (Fig. S20). As shown in Fig. 6a, both the CoP and Mo-CoP make considerable contributions to the Fermi level, manifesting admirable metallic character with zero band gaps [45]. Besides, the doping of Mo does not induce great changes in the electron arrangement of CoP. The calculated DOS of CoP and Mo-CoP suggest the different energy of Co resulted from the electron transfer between Mo and Co (Fig. 6b), as previously confirmed by XPS analysis. With Mo incorporation, the *d*-band center is upshift from the Fermi level, and the *d*-band center rises from -1.97 eV of CoP to -1.65 eV of Mo-CoP, implying an increased binding strength of H [45]. Furthermore, the substitution of Co by Mo increases the electron density around the Co atoms and decreases the surrounding electron density of Mo atoms (Fig. S21), which can accordingly lead to the thermodynamical optimization of free energy of hydrogen adsorption. Further, to elucidate the whole HER mechanism in alkaline media, we construct the reaction pathway for HER on the chosen surfaces, which is composed of bilayer adsorption of

H<sub>2</sub>O, dissociation of water to generate adsorption hydrogen (H<sup>\*</sup>) and the desorption of H<sub>2</sub> [46,47]. For the water dissociation process, the O from one of the water molecules can absorb on the Co site, while H belonging to another water molecule forms a P–H bond. The two water molecules are connected by H-bonding. On the basis of the bimolecular Volmer reaction mechanism, the Mo-CoP shows smaller free energy of H<sub>2</sub>O adsorption  $\Delta G_{H2O^*}$  of 0.36 eV than CoP (0.60 eV), suggesting an efficient water dissociation capacity, which manifests the favorable industrial prospects. Intrinsically, the electron transfer via the replacement of Co by Mo can lead to the changes of free energy of hydrogen adsorption ( $\Delta G_{H^*}$ ), which is a key descriptor in both acidic and alkaline solutions (Table S7) [38,48]. In Fig. 6c, Mo-CoP exhibits the optimal level for H<sup>\*</sup> with a decreased  $\Delta G_{H^*}$  of 0.16 eV, compared with CoP (0.30 eV). In brief, these theoretical results demonstrate the better HER activity for Mo-CoP with the  $\Delta G_{H^*}$  close to zero, consistent with experimental results.

### 4. Conclusions

In summary, the facial high-valence metal doping metallic assisted by MoO<sub>x</sub> layer derived from anodic oxidation and in situ polymerization of F on Mo-CoP nanowires was elaborated to optimize the HER activity and stability of CoP at large current density. The Mo-modulated Mo-CoP/MoO<sub>x</sub> exhibited the best HER activity with current densities of > 2000 mA cm<sup>-2</sup> at ~226 mV (alkaline) and ~275 mV (acidic) and prolonged durability. The favorable HER activity can be attributed to the adjustment of local electronic configuration and atomic arrangement of bonded Co and adjacent P atoms by high-valence Mo. This work sheds light on the general method for fine-tuning the active sites by high-valence ions at the local atomic level and the durability enhancement.

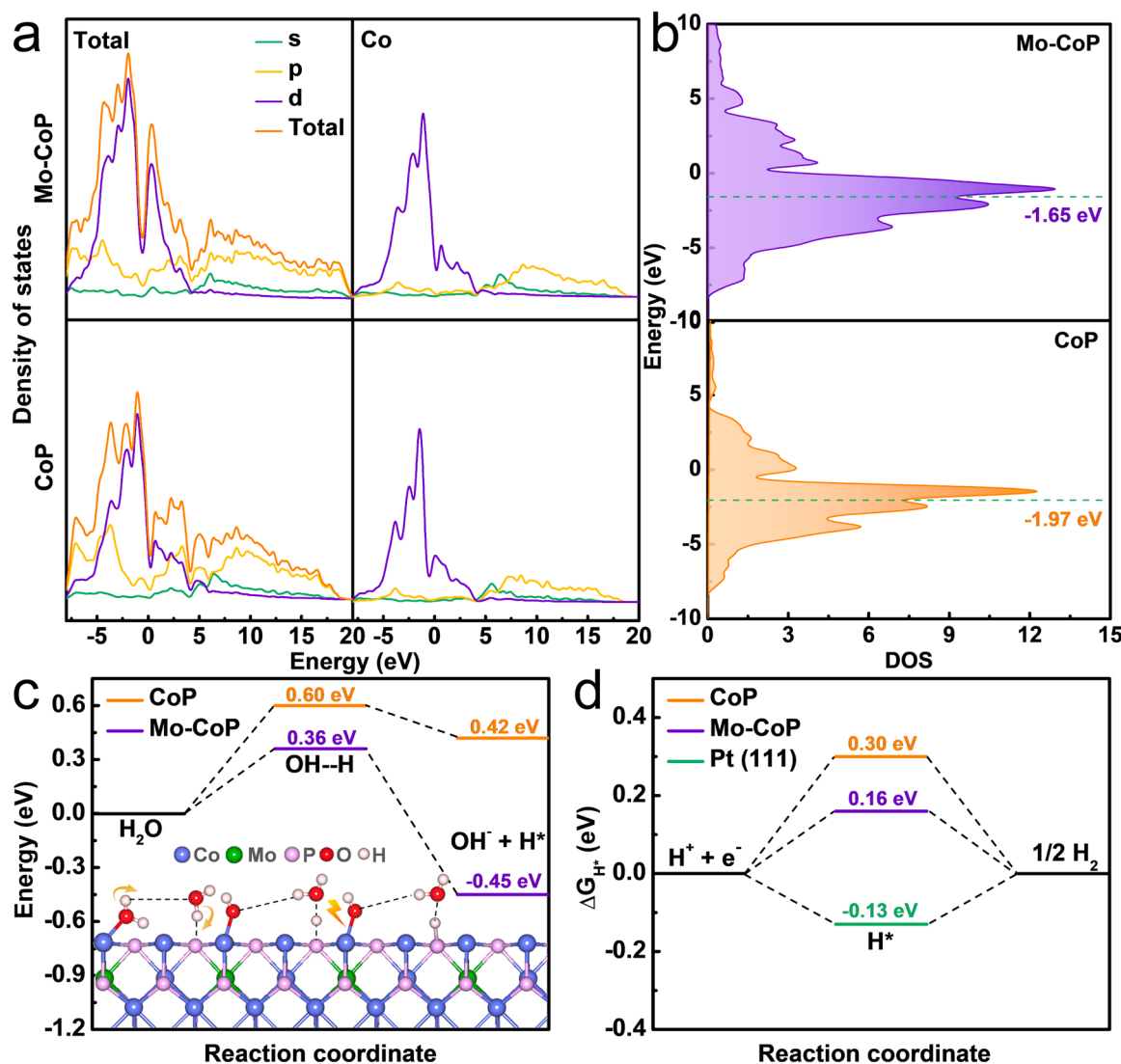


**Fig. 6.** (a) Calculated density of states and (b) d-band center level for CoP and Mo-CoP. (c) The related kinetic energy barriers for water dissociation on the surface of different catalysts. (d) Calculated free-energy diagram of HER on the surfaces of CoP and Mo-CoP at equilibrium potential.

#### CRediT authorship contribution statement

**Ya-Nan Zhou:** Data curation, Writing – original draft, Formal analysis, Investigation. **Wen-Hui Hu:** Writing – original draft, Conceptualization, Formal analysis. **Yi-Nuo Zhen:** Writing – review & editing, Formal analysis. **Bin Dong:** Formal analysis, Investigation, Resources, Writing – original draft, Funding acquisition, Project administration, Writing – review & editing. **Yi-Wen Dong:** Writing – original draft, Methodology. **Ruo-Yao Fan:** Writing – review & editing, Formal analysis. **Bin Liu:** Methodology, Writing – review & editing. **Da-Peng Liu:** Writing – original draft, Writing – review & editing. **Yong-Ming Chai:** Funding acquisition, Conceptualization, Investigation, Resources, Formal analysis, Supervision, Writing – review & editing.

#### Declaration of Competing Interest

The authors declare that they have no known competing financial interests or personal relationships that could have appeared to influence the work reported in this paper.

#### Acknowledgments

This work is financially supported by the National Natural Science Foundation of China (52174283) and Qingdao Science and Technology Benefiting People Special Project (20-3-4-8-nsh).

#### Appendix A. Supplementary material

Supplementary data associated with this article can be found in the online version at doi:10.1016/j.apcatb.2022.121230.

#### References

- [1] J. Zhou, L. Yu, Q. Zhou, C. Huang, Y. Zhang, B. Yu, Y. Yu, Ultrafast fabrication of porous transition metal foams for efficient electrocatalytic water splitting, *Appl. Catal. B Environ.* 288 (2021), 120002.
- [2] W. Zhang, W. Chen, Q. Xiao, L. Yu, C. Huang, G. Lu, A.W. Morawski, Y. Yu, Nitrogen-coordinated metallic cobalt disulfide self-encapsulated in graphitic carbon for electrochemical water oxidation, *Appl. Catal. B Environ.* 268 (2020), 118449.
- [3] Y.N. Zhou, F.L. Wang, S.Y. Dou, Z.N. Shi, B. Dong, W.L. Yu, H.Y. Zhao, F.G. Wang, J.F. Yu, Y.M. Chai, Motivating high-valence Nb doping by fast molten salt method for NiFe hydroxides toward efficient oxygen evolution reaction, *Chem. Eng. J.* 427 (2022), 131643.
- [4] Y. Ding, B.Q. Miao, S.N. Li, Y.C. Jiang, Y.Y. Liu, H.C. Yao, Y. Chen, Benzylamine oxidation boosted electrochemical water-splitting: hydrogen and benzonitrile co-

production at ultra-thin  $\text{Ni}_2\text{P}$  nanomeshes grown on nickel foam, *Appl. Catal. B Environ.* 268 (2020), 118393.

[5] J.Y. Zhang, Y. Yan, B. Mei, R. Qi, T. He, Z. Wang, W. Fang, S. Zaman, Y. Su, S. Ding, B.Y. Xia, Local spin-state tuning of cobalt-iron selenide nanoframes for the boosted oxygen evolution, *Energy Environ. Sci.* 14 (2021) 365–373.

[6] J.Y. Zhang, H. Wang, Y. Tian, Y. Yan, Q. Xue, T. He, H. Liu, C. Wang, Y. Chen, B. Y. Xia, Anodic hydrazine oxidation assists energy-efficient hydrogen evolution over a bifunctional cobalt perselenide nanosheet electrode, *Angew. Chem. Int. Ed.* 57 (2018) 7649–7653.

[7] C. Huang, L. Yu, W. Zhang, Q. Xiao, J. Zhou, Y. Zhang, P. An, J. Zhang, Y. Yu, N-doped Ni-Mo based sulfides for high-efficiency and stable hydrogen evolution reaction, *Appl. Catal. B Environ.* 276 (2020), 119137.

[8] L. Fu, Y. Li, N. Yao, F. Yang, G. Cheng, W. Luo,  $\text{IrMo}$  nanocatalysts for efficient alkaline hydrogen electrocatalysis, *ACS Catal.* 10 (2020) 7322–7327.

[9] Z.-Y. Lin, Y.-N. Zhou, J.-Y. Fu, X.-T. Yan, R.-Y. Fan, M.-X. Li, H.-J. Liu, J.-F. Yu, Y.-M. Chai, B. Dong, Ultrahigh activity of molybdenum/vanadium-doped Ni-Co phosphides nanoneedles based on ion-exchange for hydrogen evolution at large current density, *J. Colloid Interface Sci.* 604 (2021) 141–149.

[10] R. Li, H. Xu, P. Yang, D. Wang, Y. Li, L. Xiao, X. Lu, B. Wang, J. Zhang, M. An, Synergistic interfacial and doping engineering of heterostructured  $\text{NiCo}(\text{OH})\text{x}-\text{CoyW}$  as an efficient alkaline hydrogen evolution electrocatalyst, *Nano-Micro Lett.* 13 (2021) 120.

[11] X.-Q. Wang, Y.-F. Chen, B. Yu, Z.-G. Wang, H.-Q. Wang, B.-C. Sun, W.-X. Li, D.-X. Yang, W.-L. Zhang, Hierarchically porous W-Doped CoP nanoflake arrays as highly efficient and stable electrocatalyst for pH-universal hydrogen evolution, *Small* 15 (2019), 1902613.

[12] W. Zhang, B. Huang, K. Wang, W. Yang, F. Lv, N. Li, Y. Chao, P. Zhou, Y. Yang, Y. Li, J. Zhou, W. Zhang, Y. Du, D. Su, S. Guo,  $\text{WO}_x$ -surface decorated  $\text{PtNi}@\text{Pt}$  dendritic nanowires as efficient pH-universal hydrogen evolution electrocatalysts, *Adv. Energy Mater.* 11 (2021), 2003192.

[13] L. Fu, F. Yang, Y. Hu, Y. Li, S. Chen, W. Luo, Discrepant roles of adsorbed  $\text{OH}^*$  species on  $\text{IrWO}_x$  for boosting alkaline hydrogen electrocatalysis, *Sci. Bull.*, 65, 2020, pp. 1735–1742.

[14] Q.-Z. Liu, F. Jin, G.-Y. Gao, W. Wang, Ta doped  $\text{SrSnO}_3$  epitaxial films as transparent conductive oxide, *J. Alloy. Compd.* 717 (2017) 62–68.

[15] S.-M. He, Y.-Y. Meng, Q.-L. Wu, J.-L. Yang, S.-C. Huang, X.-H. Li, S.-F. Tong, T. Asefa, M.-M. Wu, Ta-Doped porous  $\text{TiO}_2$  nanorod arrays by substrate-assisted synthesis: efficient photoelectrocatalysts for water oxidation, *Nanoscale* 10 (2018) 19367–19374.

[16] B. Zhang, L. Wang, Z. Cao, S.M. Kozlov, F.P.G. Arquer, C.T. Dinh, J. Li, Z.Y. Wang, X.-L. Zheng, L.-S. Zhang, Y.-Z. Wen, O. Voznyy, R. Comin, P.-D. Luna, T. Regier, W.-L. Bi, E.E. Alp, C.-W. Pao, L.-R. Zheng, Y.-F. Hu, Y.-J. Ji, Y.Y. Li, Y. Zhang, L. G. Cavallo, H.-S. Peng, E.-H. Sargent, High-valence metals improve oxygen evolution reaction performance by modulating 3d metal oxidation cycle energetics, *Nat. Catal.* 3 (2020) 985–992.

[17] W.-X. Chen, J.-J. Pei, C.-T. He, J.-W. Wan, H.-L. Ren, Y. Wang, J.-C. Dong, K.-L. Wu, W.-C. Cheong, J.-J. Mao, X.-S. Zheng, W.-S. Yan, Z.-B. Zhuang, C. Peng, Q. Chen, D.-S. Wang, Y.-D. Li, Single tungsten atoms supported on MOF-derived N-doped carbon for robust electrochemical hydrogen evolution, *Adv. Mater.* 30 (2018), 1800396.

[18] W.-Z. Tu, K. Chen, L.-J. Zhu, H.-C.E. Zai, B. Ke, X.-X. Chen, C.-F. Sui, M.-L. Chen, Q. Y.-J. Li, Tungsten-doping-induced surface reconstruction of porous ternary Pt-based alloy electrocatalyst for oxygen reduction, *Adv. Funct. Mater.* 29 (2019), 1807070.

[19] H. Jiang, L. Yan, S. Zhang, Y. Zhao, X. Yang, Y. Wang, J. Shen, X. Zhao, L. Wang, Electrochemical surface restructuring of phosphorus-doped carbon@ $\text{MoP}$  electrocatalysts for hydrogen evolution, *Nano-Micro Lett.* 13 (2021) 215.

[20] R.Y. Fan, J.Y. Xie, H.J. Liu, H.Y. Wang, M.X. Li, N. Yu, R.N. Luan, Y.M. Chai, B. Dong, Directional regulating dynamic equilibrium to continuously update electrocatalytic interface for oxygen evolution reaction, *Chem. Eng. J.* 431 (2022), 134040.

[21] G. Qian, J. Chen, T. Yu, L. Luo, S. Yin, N-doped graphene-decorated  $\text{NiCo}$  alloy coupled with mesoporous  $\text{NiCoMoO}$  nano-sheet heterojunction for enhanced water electrolysis activity at high current density, *Nano-Micro Lett.* 13 (2021) 77.

[22] Y.-P. Liu, X. Liang, L. Gu, Y. Zhang, G.-D. Li, X.-X. Zou, J.-S. Chen, Corrosion engineering towards efficient oxygen evolution electrodes with stable catalytic activity for over 6000 h, *Nat. Commun.* 9 (2018) 2609.

[23] Y.-C. Nah, A. Ghicov, D. Kim, P. Schmuki, Enhanced electrochromic properties of self-organized nanoporous  $\text{WO}_3$ , *Electrochem. Commun.* 10 (2008) 1777.

[24] T.-H. Kim, H.J. Jeon, J.-W. Lee, Y.-C. Nah, Enhanced electrochromic properties of hybrid P3HT/ $\text{WO}_3$  composites with multiple colorations, *Electrochem. Commun.* 57 (2015) 65.

[25] W. Lee, S.-J. Park, Porous anodic aluminum oxide: anodization and templated synthesis of functional nanostructures, *Chem. Rev.* 114 (2014) 7487.

[26] P. Roy, S. Berger, P. Schmuki,  $\text{TiO}_2$  nanotubes: synthesis and applications, *Angew. Chem. Int. Ed.* 50 (2011) 2904–2939.

[27] K. Lee, A. Mazare, P. Schmuki, One-dimensional titanium dioxide nanomaterials: nanotubes, *Chem. Rev.* 114 (2014) 9385.

[28] A. Palacios-Padrós, M. Altomare, K. Lee, I. Díez-Pérez, F. Sanz, P. Schmuki, Controlled thermal annealing tunes the photoelectrochemical properties of nanochanneled Tin-oxide structures, *ChemElectroChem* 1 (2014) 1133.

[29] Y. Yang, Z.Y. Lin, S.Q. Gao, J.W. Su, Z.Y. Lun, G.L. Xia, J.T. Chen, R.R. Zhang, Q. W. Chen, Tuning electronic structures of nonprecious ternary alloys encapsulated in graphene layers for optimizing overall water splitting activity, *ACS Catal.* 7 (2017) 469–479.

[30] W.J. Li, S. Watzele, H.A. El-sayed, Y.C. Liang, G. Kieslich, A.S. Bandarenka, K. Rodewald, B. Rieger, R.A. Fischer, Unprecedented high oxygen evolution activity of electrocatalysts derived from surface-mounted metal-organic frameworks, *J. Am. Chem. Soc.* 141 (2019) 5926–5933.

[31] J.-S. Kang, J. Kim, M.J. Lee, Y.J. Son, D.Y. Chung, S. Park, J. Jeong, J.M. Yoo, H. Shin, H. Choe, H.S. Park, Y.-E. Sung, Electrochemically synthesized nanoporous molybdenum carbide as a durable electrocatalyst for hydrogen evolution reaction, *Adv. Sci.* 5 (2018), 1700601.

[32] J.Y. Cai, Y. Song, Y.P. Zang, S.W. Niu, Y.S. Wu, Y.F. Xie, X.S. Zheng, Y. Liu, Y. Lin, X.J. Liu, G.M. Wang, Y.T. Qian, N-induced lattice contraction generally boosts the hydrogen evolution catalysis of P-rich metal phosphides, *Sci. Adv.* 6 (2020) eaaw8113.

[33] Y.-Q. Sun, L.-F. Hang, Q. Shen, T. Zhang, H.-L. Li, X.-M. Zhang, X.-J. Lyu, Y. Li, Mo doped  $\text{Ni}_2\text{P}$  nanowire arrays: an efficient electrocatalyst for the hydrogen evolution reaction with enhanced activity at all pH values, *Nanoscale* 9 (2017) 16674–16679.

[34] I.H. Kwak, I.S. Kwon, T.T. Debela, H.G. Abbas, Y.C. Park, J. Seo, J.-P. Ahn, J.H. Lee, J. Park, H.S. Kang, Phase evolution of  $\text{Re}_{1-x}\text{Mo}_x\text{Se}_2$  alloy nanosheets and their enhanced catalytic activity toward hydrogen evolution reaction, *ACS Nano* 14 (2020) 11995–12005.

[35] Y. Sun, X. Ren, S. Sun, Z. Liu, S. Xi, Z.J. Xu, Engineering high-spin state cobalt cations in spinel zinc cobalt oxide for spin channel propagation and active site enhancement in water oxidation, *Angew. Chem. Int. Ed.* 60 (2021) 14536–14544.

[36] Z. Zou, J. Wang, H. Pan, J. Li, K. Guo, Y. Zhao, C. Xu, Enhanced oxygen evolution reaction of defective  $\text{CoP}/\text{MOF}$ -integrated electrocatalyst by partial phosphating, *J. Mater. Chem. A* 8 (2020) 14099–14105.

[37] L. Yan, B. Zhang, J. Zhu, Y. Li, P. Tsiaikaras, P.K. Shen, Electronic modulation of cobalt phosphide nanosheet arrays via copper doping for highly efficient neutral-pH overall water splitting, *Appl. Catal. B Environ.* 265 (2020), 118555.

[38] H.-H. Zhao, Z. Li, X.-P. Dai, M.-L. Cui, F. Nie, X. Zhang, Z.-T. Ren, Z.-H. Yang, Y.-H. Gan, X.-L. Yin, Y. Wang, W.-Y. Song, Heterostructured  $\text{CoP}/\text{MoO}_2$  on Mo foil as high-efficiency electrocatalysts for the hydrogen evolution reaction in both acidic and alkaline media, *J. Mater. Chem. A* 8 (2020) 6732–6739.

[39] Y.-R. Huang, M.-G. Li, W.-W. Yang, Y.-S. Yu, S. Hao, Ce-doped ordered mesoporous cobalt ferrite phosphides as a robust catalyst for water oxidation, *Chem. Eur. J.* 26 (2020) 13305–13310.

[40] L.K. Mishra, H.Q. Zhou, J.Y. Sun, F. Qin, K. Dahal, J.-M. Bao, S. Chen, Z.-F. Ren, Hierarchical  $\text{CoP}/\text{Ni}_3\text{P}_4/\text{CoP}$  microsheet arrays as a robust pH-universal electrocatalyst for efficient hydrogen generation, *Energy Environ. Sci.* 11 (2018) 2246–2252.

[41] J. Guo, B. Wang, D. Yang, Z. Wan, P. Yan, J. Tian, T.T. Isimjan, X. Yang, Rugae-like  $\text{Ni}_2\text{P}-\text{CoP}$  nanoarrays as a bi-functional catalyst for hydrogen generation:  $\text{NaBH}_4$  hydrolysis and water reduction, *Appl. Catal. B Environ.* 265 (2020), 118584.

[42] Z. Chen, H. Wu, J. Li, Y. Wang, W. Guo, C. Cao, Z. Chen, Defect enhanced  $\text{CoP}/$  Reduced graphene oxide electrocatalytic hydrogen production with pt-like activity, *Appl. Catal. B Environ.* 265 (2020), 118576.

[43] H. Xu, H. Jia, B. Fei, Y. Ha, H. Li, Y. Guo, M. Liu, R. Wu, Charge transfer engineering via multiple heteroatom doping in dual carbon-coupled cobalt phosphides for highly efficient overall water splitting, *Appl. Catal. B Environ.* 268 (2020), 118404.

[44] H. Jin, J. Wang, D. Su, Z. Wei, Z. Pang, Y. Wang, In-situ cobalt-cobalt oxide/N-doped carbon hybrids as superior bi-functional electrocatalysts for hydrogen and oxygen evolution, *J. Am. Chem. Soc.* 137 (2015) 2688–2694.

[45] J.Q. Zhang, X. Shang, H. Ren, J.Q. Chi, H. Fu, B. Dong, C.G. Liu, Y.M. Chai, Modulation of inverse spinel  $\text{Fe}_3\text{O}_4$  by phosphorus doping as an industrially promising electrocatalyst for hydrogen evolution, *Adv. Mater.* 31 (2019), 1905107.

[46] J. Durst, A. Siebel, C. Simon, F. Hasche, J. Herranz, H.A. Gasteiger, Hydrogen oxidation and evolution reaction mechanism, *Energy Environ. Sci.* 7 (2014) 2255–2260.

[47] P. Dementyev, K.H. Dostert, F. Ivars-Barcelo, C.P. O'Brien, F. Mirabella, S. Schauerermann, X. Li, J. Paier, J. Sauer, H.J. Freund, Water interaction with iron oxides, *Angew. Chem. Int. Ed.* 127 (2015) 14148–14152.

[48] T. Liu, P. Li, N. Yao, G.Z. Cheng, S.L. Chen, W. Luo, Y.D. Yin, CoP-doped MOF-based electrocatalyst for pH-universal hydrogen evolution reaction, *Angew. Chem. Int. Ed.* 58 (2019) 4679–4684.